Interface properties of Ti3SiC2/Al2O3 ceramics: Combined experiments and first-principles calculations

Ji, Jun; Yu, Jinman; Lee, Bill; Middleburgh, Simon; Li, Dechun; Wang, Xuye; Li, Qinggang; Wang, Zhi; Shi, Guopu; Chen, Fei; Zhang, Liu

Ceramics International

DOI:
10.1016/j.ceramint.2020.10.221

Published: 01/03/2021

Peer reviewed version

Interface properties of Ti_3SiC_2/Al_2O_3 ceramics: Combined experiments and first-principles calculations

Jun Ji[a], Liu Zhang[b], Jinman Yu[a], William E. Lee[c], Simon C. Middleburgh[c], Dechun Li[d], Xuye Wang[a], Qinggang Li[a], Zhi Wang[a*], Guopu Shi[a**],Fei Chen[e]

[a]*School of Material Science and Engineering, University of Jinan, Jinan 250022, China*

[b]*School of materials science and Engineering，Yancheng Institute of Technology，Yancheng 224051，China*

[c]*Nuclear Futures Institute, Bangor University, Bangor, Gwynedd LL57 2DG, United Kingdom*

[d]*School of Information Science and Engineering, Shandong University, Qingdao 266237, China.*

[e]*State Key Laboratory of Advanced Technology for Materials Synthesis and Processing,Wuhan University of Technology, Wuhan 430070, China*

[*] *First corresponding author: wangzhi@ujn.edu.cn*

[**] *Second corresponding author: ss_shigp@ujn.edu.cn;*

Abstract

The synthesis, characterization, and first-principles calculations of Ti_3SiC_2/Al_2O_3 ceramics were reported. X-ray diffraction measurements showed that the composite ceramics were highly pure. Scanning electron microscopy and transmission electron microscopy were used to characterize the interface information for Ti_3SiC_2 and Al_2O_3 crystals. Surface energies and interface properties were calculated using the first-principles method. The results suggested that Ti_3SiC_2 with Ti terminations and Al_2O_3 with O terminations are more stable than other terminations crystals. Thus powerful attraction between the coordinatively unsaturated Ti and O atoms on the Ti_3SiC_2‖ Al_2O_3 interface would result in higher work of adhesion (Wad) and shorter boundary distance, demonstrating the intercrystalline strengthening of Ti_3SiC_2/Al_2O_3 composite ceramics.

Keywords: *Ti_3SiC_2/Al_2O_3 ceramics; first-principles calculations; interface properties*

1. Introduction[1]

Alumina ceramics, which exhibit high hardness, suitable flexure strength, and

[1] Abbreviations:

DFT	Density functional theory
EDS	Energy-dispersive X-ray spectroscopy
SEM	Scanning electron microscopy
TEM	Transmission electron microscopy
UBER	Universal binding energy relation
XRD	X-ray diffraction

high chemical stability, have attracted significant attention in recent years, and as a result, they have been commonly used in industry[1–3]. However, their low fracture toughness limits their further development as a reliable ceramic material[4], and therefore, a novel material should be designed to address this issue[5,6]. For example, self-toughening Al_2O_3 ceramics[7], graphene nanoplate-toughened Al_2O_3-based ceramics[8], and multiwalled carbon nanotube-toughened Al_2O_3-based ceramics[9], have been prepared and found to exhibit good mechanical properties.

In addition, MAX phases (M = early transition metal; A = main group element; X = C or N), which were first reported by Jeitschko and Nowotny in the 1960s, have received considerable attention in recent years[10-13]. To date, more than 150 types of MAX phases have been discovered, most of which belong to the 211[14-16], 312[17-19], and 413[20-22] phases, and their properties have been investigated. In the case of the 312 phase, Ti_3SiC_2[23], Ti_3AlC_2[24], and Ti_3GeC_2[25] have been widely applied owing to their facile preparation and excellent stability. In particular, Ti_3SiC_2 contains strong covalent Ti-C bonds and weak metallic Ti-Si bonds, thereby resulting in a combination of ceramic and metallic properties[26,27], indicating its potential to act as a toughening phase in alumina ceramics. Recently, our group synthesized Ti_3SiC_2/Al_2O_3 ceramic composites and found a clear boundary between the Ti_3SiC_2 and Al_2O_3 crystal surfaces, in addition to improved mechanical properties compared to the Al_2O_3 system alone[4,28]. First-principles calculations, which can be used to reveal the atomic and electronic structures of crystals, are widely employed in the study of MAX phases[29,30], such as in the study of solid solutions[18,31], surface

properties, and interface properties[32]. However, although the surface properties of Ti_3SiC_2 (0 0 1) have been calculated[33], the interface properties between Ti_3SiC_2 and Al_2O_3 have not yet to be clearly identified.

Thus, we herein report the preparation of Ti_3SiC_2/Al_2O_3 ceramic composites via the hot-pressing sintering method. In addition, the composition and morphological characteristics of the Ti_3SiC_2 and Al_2O_3 grains are investigated via X-ray diffraction (XRD), scanning electron microscopy (SEM), and transmission electron microscopy (TEM). Furthermore, first-principles calculations are used to explore the accurate surface/interface structure and features of the Ti_3SiC_2 and Al_2O_3 crystals. To the best of our knowledge, this is the first report into the properties of the Ti_3SiC_2/Al_2O_3 interface with the aim of supporting the mechanism of boundary strengthening in composite ceramics.

2. Materials and methods

2.1 Experimental method

The raw materials employed herein were fine powders. Sample 1 was obtained by means of the following. Dry 50 vol% Al_2O_3 (18.6 g, 99.6 wt% pure, particle size was approximately 0.5 μm) and 50 vol% Ti_3SiC_2 (21.4 g, 99 wt% pure, particle size was approximately approximately 0.5 μm) were dispersed evenly in ethanol at 200 rpm for 4 h in a planetary mill (XQM-2, Changsha Tianchuang Powder Technology Co. LTD, China), following which the resulting slurry was dried in a drying oven at 70 °C and sieved using a 50 mesh sifter. Subsequently, the raw materials were sintered

in a vacuum hot-pressing furnace (VVPgr-80–2300, Shanghai Haoyue Electric Furnace Technology Co. LTD, China) at 1450 ℃ for 1.5 h under a vacuum pressure of $<8.0\times10^{-3}$ MPa, and the pressure was maintained at 30 MPa below uniaxial pressure when the sintering temperature was 1450 ℃. Finally, the sintered bulk were allowed to cool naturally to room temperature prior to their removal from the furnace.

The obtained sample 1 was polished using SiC powder and then cut into 3 mm × 4 mm × 3 mm rectangular solid using an inner circle cutting machine (J5090, Shenyang Kejing Automation equipment Co. LTD, China). It was then cleaned using ultrasonication in ethanol for 20 min. Phase compositions of the obtained sample was determined by XRD (D8 ADVANCE, Bruker, Germany). and mass fraction was calculated approximately using the K value method:

$$W_X = I_{Xi} \Big/ \sum_{i=A}^{N} \frac{I_i}{K_A^i} \qquad (1)$$

where W_x is the mass faction of the X phase, I_{xi} represents the highest peak value of the X phase, and K^i_A can determined via RIR (3.69 for Ti_3SiC_2 and 1.01 for Al_2O_3 according to the standard PDF#74-0310 and 71-1683 respectively). TEM specimens were prepared by cutting to the thickness of <5 μm and then undergoing argon-ion milling. Microstructural investigations were performed by TEM (JSM-2100F, JEOL, Japan) operated at 200kV and SEM (JSM-7610F, JEOL, Japan) with an energy dispersive spectroscopy (EDS) after coating Au on measurement surface for 30S.

2.2 Theoretical method

First-principles calculations were performed using the plane-wave CASTEP codes based on the density functional theory (DFT) approach. The electron exchange-correlation was described using the GGA-PBE functional. The plane-wave ultrasoft pseudopotential methods were exploited to present the interactions between the electrons and the ion cores. A variety of plane-wave cutoff energies and k-points were used as listed in Tab. S1 and S2, which included 15 surface/ interface models respectively. A vacuum layer of 15 Å was selected to prevent unwanted interactions between the surface atoms. The initial optimal interface layer thickness was calculated using the universal binding energy relations method (UBER). All models were relaxed until the forces on each atom were <0.03 eV/Å, and the stress on each atom was converged to 0.05 GPa. The maximum atom displacement was set at 0.001 Å, and the total energy changes during the optimization finally converged to 10^{-5} eV/atom.

3. Results and discussion

3.1 Composition and microstructural properties

Sample 1 was synthesized from Al_2O_3 and Ti_3SiC_2 powder. The phase compositions of the obtained Ti_3SiC_2/Al_2O_3 ceramics were analyzed through XRD (Fig. 1), where strong peaks corresponding to Ti_3SiC_2 and Al_2O_3 were clearly shown. The TiC peaks were not observed in sample 1, indicating that Al_2O_3 and Ti_3SiC_2 were stable and did not reacted with each other. The contents of Al_2O_3 and Ti_3SiC_2 were 46.2 wt% and 53.8 wt%, respectively by calculation of eq. (1).

Fig. 2a shows the fracture surface of sample 1. As can be seen, the particle diameters of the Ti_3SiC_2 and Al_2O_3 grains are approximately 2–3 μm, with no abnormal growth being observed. In addition, the interface combination is close and no obvious pores are present, thereby revealing the sintering densification of such Ti_3SiC_2/Al_2O_3 ceramics. Furthermore, the energy-dispersive X-ray spectroscopy (EDS) mapping images are presented in Fig. 2b, indicating that two types of grain are present, and the aggregation of Si and TiC does not occur, as also suggested by the XRD results.

Grains morphology could be simulated by Morghology module. As can be seen in Fig. S1, Ti_3SiC_2 crystal exhibits plate-like shape and (0 0 1) as well as (1 0 0) planes are main exposed surfaces. While for Al_2O_3 crystal, (0 0 1) and (0 1 2) planes consist outside surfaces. Fig. 3 shows the different interface morphologies of two neighboring grains in the Ti_3SiC_2/Al_2O_3 composite. More specifically, In Fig. 3a, the black crystal represents a Ti_3SiC_2 grain, whereas the Al_2O_3 particles are gray in color. The interface boundaries between two grains are clear and straight. Furthermore, selected area electron diffraction (SEAD) analysis of the area indicated by the red oval is shown in Fig. 3b. For Ti_3SiC_2, the d-spacings of the three diffraction spots are 0.824, 0.264, and 0.244 nm respectively, which are consistent with the (0 0 2), (1 0 0), and (1 0 2) crystal planes of the Ti_3SiC_2 grains. Similarly, the (0 0 6), (0 2 4), and (0 2 10) crystal planes of the Al_2O_3 particles are also indicated. The dihedral angle between Ti_3SiC_2 (1 0 0) and Al_2O_3 (0 0 6) is approximately 180°, which suggests that the orientation relationship is Ti_3SiC_2 (1 0 0)∥ Al_2O_3 (0 0 1). The incident beam is parallel

to the [0 1 0] axis of Ti_3SiC_2 and the [1 0 0] axis of the Al_2O_3 crystal. Fig. 3c shows the lattice fringes of Ti_3SiC_2 (0 0 1) and Al_2O_3 (0 1 2), whereby the parallel crystal planes clearly indicate the interface composition of Ti_3SiC_2 (0 0 1)∥ Al_2O_3 (0 1 2).

3.2 Lattice parameters and surface properties of Ti_3SiC_2 and Al_2O_3

The lattice parameters of Ti_3SiC_2 and Al_2O_3 by first-principles calculations are listed in Tab. 1. The calculated results are in agreement with the standard PDF#74-0310 (Ti_3SiC_2) and 71-1683 (Al_2O_3), thereby indicating the reliability of the simulation methods and the calculation parameters.

Table 1. Lattice parameters and bond lengths for Ti_3SiC_2 and Al_2O_3

Ti_3SiC_2		Al_2O_3	
a/Å	3.078	a/Å	4.816
c/Å	17.621	c/Å	13.132
c/a	5.724	c/a	2.73
Ti1-C/Å	2.191	Al1-O/Å	1.874
Ti2-C/Å	2.102	Al2-O/Å	1.996
Ti2-Si/Å	2.681		

In terms of the crystal growth morphology, the outside surfaces are composed of the (1 0 0) and (0 0 1) planes for Ti_3SiC_2, and the (0 0 1) and (0 1 2) planes for the Al_2O_3 grains, which is also observed by TEM images. Thus, the pair-combinations of these four surfaces would be expected to form the main interface in Ti_3SiC_2/Al_2O_3 ceramics. As such, prior to investigation of the interface properties, the surface energies of the above four planes should be considered.

As shown in Fig. 4, six models of the Ti_3SiC_2 (0 0 1) plane with different

terminations were established, i.e., (a) Ti1(C); (b) C(Ti2); (c) Ti2(Si); (d) Si(Ti2); (e) Ti2(C); and (f) C(Ti1). For example, the Ti1(C) termination indicates that the surface atom is Ti1 and the subsurface atom is C. In addition, Fig. S2 shows three models of the Ti_3SiC_2 (1 0 0) plane, and Fig. S3 shows six slabs of the Al_2O_3(0 0 1) and (0 1 2) planes. In total, 15 surface models were obtained for the subsequent surface energy calculations.

Surface relaxation is an important feature of the surface structure. Owing to the unsaturated bonds of surface atoms, they tend to move to new positions to reduce the energy. Surface convergence tests were therefore conducted to ensure that the slabs would in accord with bulk-like interiors. The interlayer relaxation can be evaluated as follows:

$$\Delta d_{ij} = {}^{(d_{ij}-d_{ij,bulk})}\!\Big/_{d_{ij,bulk}} \times 100\% \qquad (2)$$

where $d_{ij,bulk}$ and d_{ij} represent the distance between the *ith* and *jth* layers in the bulk and after relaxation, respectively. A positive value for Δd_{ij} indicates layer expansion, whereas a negative value indicates contraction. Because a number of structural model thicknesses were tested, only the changes in the innermost interlayers are listed in Tab. S3. As can be seen, the Δd of the innermost interlayer is particularly low, which indicates that the slab is sufficiently thick to meet the bulk properties. Additional investigations into the MAX phase surface relaxation can be found in the literature [15,16,32,33].

On the surface, a variety of terminations will lead to different surface energies, and therefore, it is necessary to understand which type of termination is the most

stable. The surface energies for the different terminations can be calculated as follows:

$$E_{surf} = \frac{1}{2A}(E_{slab} - N_{Ti}\mu_{Ti} - N_{Si}\mu_{Si} - N_C\mu_C - PV - TS) \quad (3)$$

where A represents the surface area, E_{slab} is equal to the total energy of the slab, N_{Ti}, N_{Si}, and N_C are the number of Ti, Si, and C atoms in the slab, respectively, μ_{Ti}, μ_{Si}, and μ_C are the chemical potentials of the Ti, Si, and C atoms in the slab, respectively, and V and S are the volume and entropy of the system, respectively. At 0 K and a low pressure, the values of PV and TS can be neglected. The total chemical potentials of the surface system $\mu_{Ti_3SiC_2}$ are therefore equal to the bulk energy $E^{bulk}_{Ti_3SiC_2}$, and $\mu_{Ti_3SiC_2}$ is the sum of the Ti, Si, and C chemical potentials, which can be expressed as

$$E^{bulk}_{Ti_3SiC_2} = \mu_{Ti_3SiC_2} = 3\mu_{Ti} + \mu_{Si} + 2\mu_C \quad (4)$$

Thus, Eq.(4) becomes

$$E_{surf} = \frac{1}{2A}[E_{slab} - \frac{1}{2}N_C E^{bulk}_{Ti_3SiC_2} - \mu_{Ti}(N_{Ti} - \frac{3}{2}N_C) - \mu_{Si}(N_{Si} - \frac{1}{2}N_C)] \quad (5)$$

For a stoichiometric surface, $2N_{Ti} = 3N_C$, $2N_{Si} = N_C$, and thus,

$$E_{surf} = \frac{1}{2A}(E_{slab} - \frac{1}{2}N_C E^{bulk}_{Ti_3SiC_2}) \quad (6)$$

For a non-stoichiometric surface, $2N_{Ti} \neq 3N_C$, $2N_{Si} \neq N_C$, and therefore, the chemical potentials of Ti and Si would influence the surface energy value. Due to the stabilities of the sample substances, the chemical potentials of Ti and Si in the slab must be lower than those in the bulk. The maximum values of the chemical potentials for Ti, Si, and C can be represented as

$$\Delta\mu_{Ti} = \mu_{Ti} - E_{Ti}^{bulk} \le 0 \qquad (7)$$

$$\Delta\mu_{Si} = \mu_{Si} - E_{Si}^{bulk} \le 0 \qquad (8)$$

$$\Delta\mu_{C} = \mu_{C} - E_{C}^{bulk} \le 0 \qquad (9)$$

where $\Delta\mu_{Ti}$, $\Delta\mu_{Si}$, and $\Delta\mu_{C}$ represent the changes in chemical potential between the sample elements and the pure bulks of Ti, Si, and C, where E_{Ti}, E_{Si}, and E_{C} are the energies of the bulk hcp-Ti, fcc-Si, and diamond C, respectively. Through a combination of Eqs (4), (7), (8), and (9),

$$3\Delta\mu_{Ti} + \Delta\mu_{Si} \ge E_{Ti_3SiC_2}^{bulk} - (3E_{Ti}^{bulk} + E_{Si}^{bulk} + 2E_{C}^{bulk}) \qquad (10)$$

where

$$E_{Ti_3SiC_2}^{f} = 3E_{Ti}^{bulk} + E_{Si}^{bulk} + 2E_{C}^{bulk} - E_{Ti_3SiC_2}^{bulk} \qquad (11)$$

In this case, E^f is the formation energy of Ti_3SiC_2 is 5.4 eV. Finally, the following surface energy equations can be obtained:

$$E_{surf} = \frac{1}{2A}[E_{slab} - \frac{1}{2}N_C E_{Ti_3SiC_2}^{bulk} - E_{Ti}^{bulk}(N_{Ti} - \frac{3}{2}N_C) - E_{Si}^{bulk}(N_{Si} - \frac{1}{2}N_C)$$
$$- \Delta\mu_{Ti}(N_{Ti} - \frac{3}{2}N_C) - \Delta\mu_{Si}(N_{Si} - \frac{1}{2}N_C)] \qquad (12)$$

Because the non-stoichiometric surface energy is a function of $\Delta\mu$Ti and $\Delta\mu$Si, it is a range based on the change in chemical potential, rather than a definite value. By the same method, the surface energy of Al_2O_3 can be obtained as

$$E_{surf} = \frac{1}{2A}[E_{slab} - \frac{1}{2}N_{Al}E_{Al_2O_3}^{bulk} - E_{O}^{bulk}(N_O - \frac{3}{2}N_{Al}) - \Delta\mu_O(N_O - \frac{3}{2}N_{Al})] \qquad (13)$$

For simplification, the means of the parameters for Al_2O_3 above are omitted, and the E^f value of Al_2O_3 is calculated to be 15.65 eV.

Thus, as derived from Eqs (12) and (13), the surface energies $E_{Ti_3SiC_2}$ and $E_{Al_2O_3}$ are functions of $\Delta\mu_{Ti}$, $\Delta\mu_{Si}$, and $\Delta\mu_{O}$.

Fig. 5a shows the surface energy of Ti_3SiC_2 (0 0 1) with variation in $\Delta\mu_{Ti}$, and $\Delta\mu_{Si}$ fixed at zero. As can be seen from this figure, the surface energies of the C(Ti1) and C(Ti2) terminations are significantly higher than those of the other four terminations over the whole range of $\Delta\mu_{Ti}$, which demonstrates that both termination surfaces are unstable. In contrast, the surface energies of the Si(Ti2) and Ti2(C) terminations are constant, and the other four surface energies are linearly dependent on $\Delta\mu_{Ti}$. Upon increasing the value of $\Delta\mu_{Ti}$, the surface energies of the Ti2(Si) and Ti1(C) terminations decrease, and the values of both reach minimum when $\Delta\mu_{Ti}$ at zero, thereby suggesting that the Ti2(Si) and Ti1(C) terminations produce the most stable surface. In addition, Fig. 5b shows the surface energy of Ti_3SiC_2 (0 0 1) whereby $\Delta\mu_{Si}$ was varied while $\Delta\mu_{Ti}$ was unchanged at zero. As indicated, the Ti1(C) and C(Ti2) terminations are independent of the range of $\Delta\mu_{Si}$. It was found that the C(Ti1) and Ti2(C) termination surface energies increased while those of the Ti2(Si) and Si(Ti2) terminations decreased as $\Delta\mu_{Si}$ was increased to zero. The results presented in Fig. 5 therefore indicates that the Ti1(C) and Ti2(C) terminations are more stable over the ranges of $\Delta\mu_{Ti}$ and $\Delta\mu_{Si}$ examined herein. Furthermore, Fig. S4a and S4b show the surface energy of Ti_3SiC_2 (1 0 0) where $\Delta\mu_{Ti}$ and $\Delta\mu_{Si}$ are both varied, and in both cases, the C(Ti2) terminations are constant, the C(Ti1) termination surface energy increases, and the (Ti-Si) termination surface energy decreases upon increasing $\Delta\mu_{Ti}$ and $\Delta\mu_{Si}$. This indicates the superior stability of the (Ti-Si) termination surface. Moreover, Fig. S4c shows the Al_2O_3 (0 0 1) and (0 1 2) surface energies as a function of $\Delta\mu_O$. As indicated, the surface energies for (0 0 1)-Al1 and

(0 1 2)-Al are independent of $\Delta\mu_O$, the (0 0 1)-O and (0 1 2)-O1 terminations show reduced values, and those for the (0 0 1)-Al2 and (0 1 2)-O2 termination increase upon increasing $\Delta\mu_O$. In total, the five most stable termination surfaces present in the Ti_3SiC_2 and Al_2O_3 grains are -Ti1(C) and -Ti2(C) for the Ti_3SiC_2 (0 0 1) plane, -Ti-Si for the Ti_3SiC_2 (1 0 0) plane, and (0 0 1)-Al1 and (0 1 2)-O1 for the Al_2O_3 grain. For simplicity, we named Ti_3SiC_2 (0 0 1)-Ti1(C) as TSC (0 0 1)-Ti1, Ti_3SiC_2 (0 0 1)-Ti2(C) as TSC (0 0 1)-Ti2, Ti_3SiC_2 (1 0 0)-Ti-Si as TSC (1 0 0), Al_2O_3 (0 0 1)-Al1 as AO (0 0 1), and Al_2O_3 (0 1 2)-O1 as AO (0 1 2).

Fig. 6 shows the differences in electron density for the five low energy planes. More specifically, for the TSC(0 0 1)-Ti1 terminations (model a), surface relaxation causes significant variations in the charge distribution on the surface area, whereas for the TSC(0 0 1)-Ti2 and TSC(1 0 0) terminations (models b and c), the electron density increases between the surface Ti and subsurface C layers, suggesting that the Ti-C chemical bond is strengthened after relaxation. In the case of the AO(0 0 1) terminations (model d), due to convergence of the surface Al atoms to the subsurface O layer, the electron density increases around the subsurface O atoms while reducing around the Al atoms. In addition, no significant changes were observed for the AO(0 1 2) terminations (model e), and the charge difference was distributed uniformly both in the bulk and at the surface, thereby suggesting that the AO(0 1 2) terminations presented little influence following relaxation when compared to the other four models. Tab. S4 lists average bond lengths of Ti-C, Ti-Si and Al-O in surface/bulk models. The shorter bond lengths indicates the surface contraction after relaxing,

which is in accord with the inference deduced from Fig.6.

3.3 Interface properties in Ti_3SiC_2/ Al_2O_3 ceramics

Based on the above discussion, five stable surfaces with different crystal planes or terminations were selected to construct the interface models, thereby resulting in the preparation of fifteen interface models. Due to the different surface models have inconsistant lattice parameters (e.g., Ti_3SiC_2 (0 0 1) plane, U = V = 3.759 Å; Al_2O_3 (0 0 1) plane, U = V = 4.578 Å), if the two surfaces combine directly, the Ti_3SiC_2 unit cell would suffer tension force and the Al_2O_3 unit cell would be exposed to stress, giving a mismatch rate of close to 20%. That does not truly represent the interface environment. As can be seen in Fig. 7, a supercell was built using a 3×3 unit cell for Ti_3SiC_2 (0 0 1) and a 2×2 for Al_2O_3 (0 0 1), and the revised lattice parameters are U = V = 9.201 Å for Ti_3SiC_2 (0 0 1) and U = V = 9.518 Å for Al_2O_3 (0 0 1). This resulted in a reduction in the mismatch rate to 1.7%, thereby suggesting that this interface model (U = V = 9.359 Å) could approximately reflect the real interface structure.

Thus, the unit cell and supercell parameters, and mismatch rates of the fifteen established interface models are presented in Tab. S5. As can be seen from the data presented, the maximum mismatch rate is 3.7% for Ti_3SiC_2 (1 0 0)‖ Al_2O_3 (0 1 2) along the V direction. The low mismatch rates for interface models indicate that they are able to accurately reflect the data of Ti_3SiC_2‖ Al_2O_3 interfaces. Figures S4, S5, and S6 show the fifteen interface structures models in total.

To optimize the interface distance between two surfaces, the dependence of the interface energy on the surface distance was plotted using the UBER method, as

shown in Fig. S8. The stability of the interface can be qualitatively expressed by the work of adhesion (W_{ad}):

$$W_{ad} = (E_a^{slab} + E_b^{slab} - E_{a/b}^{slab}) / A \qquad (14)$$

where E^{slab}_a, E^{slab}_b are the energies of surface models a and b, respectively, $E^{slab}_{a/b}$ is the energy of the interface model composed of a and b, A represents the interface area, and W_{ad} is defined as the reversible work per unit area to divide an interface into two free surfaces. As can be seen from Fig. S8, the approximately optimized interface distance (d_0) can be predicted using the UBER method, corresponding to the minimum value of the total energy. To improve its efficiency, the UBER method is a coarse method with constrained atoms, and therefore, the subsequent step involves geometry optimization starting from d_0 and full relaxation. Finally, W_{ad} can be calculated using Eq. (14). The corresponding values of W_{ad} and the interface distance for the fifteen interface models are presented in Fig. 8.

As can be seen from Fig. 8A, models (a–g) represent the six interface models of Ti_3SiC_2 and Al_2O_3, where the W_{ad} value ranging from 3.88 to 5.95 J/m^2 suggests that the interfaces of Ti_3SiC_2 and Al_2O_3 exhibit the highest stabilities of the various models. By contrast, the lower average W_{ad} values of 1.92 and 3.13 J/m^2 for Al_2O_3‖ Al_2O_3 (g–i) and Ti_3SiC_2‖ Ti_3SiC_2 (k–p) respectively, indicate their lower interface stabilities compared to Ti_3SiC_2‖ Al_2O_3. The interface distances were also measured, as shown in Fig. 8B. Thus, the higher d values of models (a) and (b) (i.e., 1.98 and 2.08 Å, respectively) indicate the presence of weaker binding forces between Ti_3SiC_2 (0 0 1)-Ti and Al_2O_3 (0 0 1)-Al. The interface distances of <1.5 Å measured for models c–f

suggest strong binding forces at the interface, which correspond to the high W_{ad} values. In addition, the interface distances of models (g–p) generally range from 2.0 to 2.8 Å, with the exception (h) and (n), whose d values of 1.85 and 1.56 Å, respectively. Although short distances were found for Al_2O_3 (0 1 2)‖ Al_2O_3 (0 1 2) and Ti_3SiC_2 (1 0 0)‖ Ti_3SiC_2 (1 0 0) (models n and h respectively), their W_{ad} values did not display any significant increase, thereby suggesting that compared to Ti_3SiC_2‖ Al_2O_3, the binding forces of Al_2O_3‖ Al_2O_3 and Ti_3SiC_2‖ Ti_3SiC_2 are significantly weaker.

The distance between the surface and the subsurface layer would be expected to change upon the formation of a stable boundary. Thus, as shown in Fig. S9, the majority of surface layers expand in the Al_2O_3 (0 1 2) plane. In models (h), (i), (d), (e), and (f), the expansion ratios are 16.8%, 55.2%, 88.7%, 97.2%, and 101.8% respectively, which suggest that the O atoms are susceptible to their interface surroundings.

More specifically, Fig. 9 shows the differences in electron density following geometry optimization of the interface models. Because of the similar differences in the electron densities of the Al_2O_3‖ Al_2O_3 and Ti_3SiC_2‖ Ti_3SiC_2 interfaces, we only selected models (m) and (h) to display. It is clear that the transferred charge is focused on the interface of Ti_3SiC_2‖ Al_2O_3, whereas the electron density remains mostly stable at the Al_2O_3‖ Al_2O_3 and Ti_3SiC_2‖ Ti_3SiC_2 interfaces. Notably, the O atom layer is more likely to expand when the Al_2O_3 (0 1 2) surface meets the Ti_3SiC_2 (0 0 1) and (1 0 0) planes, and the average distance between Ti and O atoms was calculated to be 1.75 Å, which corresponds with the Ti-O bond length. Therefore, these data indicate

that the high work of adhesion and short interface distance of Ti_3SiC_2‖ Al_2O_3 are derived from the strong attraction of unsaturated coordinated Ti and O atoms at the interface.

4. Conclusions

We herein reported the syntheses of Ti_3SiC_2/Al_2O_3 ceramics using Ti_3SiC_2 and Al_2O_3 powders. XRD and SEM observations indicated that the samples were essentially free from TiC impurity. Based on TEM observations and analysis of the related literature, surface and interface models were established. The surface energies of the Ti_3SiC_2 (001) and (100) planes as well as the Al_2O_3 (001) and (012) planes were calculated by first-principles calculations. From a thermodynamics point of view, (001)-Ti1(C), Ti2(C), and (100)-Ti-Si terminations for Ti_3SiC_2 crystal and (001)-Al1 and (012)-O terminations for Al_2O_3 crystal presented low surface energies, indicating that these five surface slabs are more stable than the other planes examined. As a result, the main interfaces of the Ti_3SiC_2/Al_2O_3 ceramics are composed of these five surface models, and the work of adhesion (W_{ad}) was calculated for each. It was found that the W_{ad} value between Ti_3SiC_2 and Al_2O_3 was higher than those of Ti_3SiC_2‖ Ti_3SiC_2 and Al_2O_3‖ Al_2O_3, suggesting that the interface between Ti_3SiC_2 and Al_2O_3 is stronger. Charge distribution measurements confirmed that the electron density would improve considerably upon formation of the Ti_3SiC_2‖ Al_2O_3 interface owing to the strong attraction between unsaturated coordinated Ti and O atoms at the interface. To the best of our knowledge, this is the first report into the interface

properties of the Ti_3SiC_2/Al_2O_3 ceramics with the aim of supporting the mechanism of boundary strengthening in composite ceramics.

Acknowledgements

Authors appreciate the financial supported by the National Natural Science Foundation of China (Grant No. 51872118, 51701081), the Key Research and Development Program of Shandong Province (Grant No. 2019GGX104077, 2019RKB01018), the Shandong Provincial Natural Science Foundation, (Grant No. ZR2018PEM008, ZR2019MEM055). The project supported by State Key Laboratory of Advanced Technology for Materials Synthesis and Processing (Wuhan University of Technology). This work was financially supported by National Natural Science Foundation of China (51632003), the Taishan Scholars Program, and the Case-by-Case Project for Top Outstanding Talents of Jinan.

References

[1] M.N. Rahaman, A. Yao, B.S. Bal, J.P. Garino, M.D. Ries, Ceramics for prosthetic hip and knee joint replacement. J. Am. Ceram. Soc. 90 (2007) 1965–1988.

[2] Y. Cai, H. Yin, L. Pan, P. Chen, G. Sun, Microstructures and mechanical properties of Ti_3SiC_2/TiC-Al_2O_3 composites synthesized by reactive hot pressing. Mater. Sci. Eng. A. 571 (2013) 137–143

[3] T.D. Dao, H.I. Lee, M.J. Han, Alumina-coated graphene nanosheet and its composite of acrylic rubber, J. Colloid Interf. Sci. 416(4) (2014) 38–43.

[4] F.F. Qi, G.P. Shi, K. Xu, T. Su, Z. Wang, J.Y. Wu, Q.G. Li, H. Wu, L. Zhang, R.C.

Zhu, B.Z. Yang, Microstructure and mechanical properties of hot pressed Ti_3SiC_2/Al_2O_3, Ceram. Int. 45 (2019) 11099–11104. .

[5] S.M. Naga, A. M. Hassan, M. Awaad, Physical and mechanical properties of Ta_2O_5 doped zirconia-toughened alumina (ZTA) composites, Ceram. Int. 41 (2015) 6248–6255.

[6] H. Wu, G. Fan, An overview of tailoring strain delocalization for strength-ductility synergy, Prog. Mater. Sci. 113 (2020) 100675, https://doi.org/10.1016/j.pmatsci.2020.100675.

[7] W. He, Y.L. Ai, B.L. Liang, W.H. Chen, C.H. Liu, Effects of La_2O_3 and Nb_2O_5 dopants on the microstructural development and fracture toughness of Al_2O_3 ceramic, Mater. Sci. Eng. A. 723 (2018) 134–140.

[8] X.L. Meng, C.H. Xu, G.C. Xiao, M.D. Yi, Y.B. Zhang, Microstructure and anisotropy of mechanical properties of graphene nanoplate toughened Al_2O_3-based ceramic composites, Ceram. Int. 42 (2016) 16090–16095.

[9] K. Ahmad, W. Pan, Microstructure-toughening relation in alumina based multiwall carbon nanotube ceramic composites, J. Eur. Ceram. Soc. 35 (2015) 663–671.

[10] A.G. Zhou, C.A. Wang, Y. Huang, A possible mechanism on synthesis of Ti_3AlC_2, Mater. Sci. Eng. A. 352 (2003) 333–339.

[11] Z.M. Liu, E.D. Wu, J.M. Wang, Y.H. Qian, H.M. Xiang, X.C. Li, Q.Q. Jin, G.A Sun, X.P. Chen, J.Y. Wang, M.S. Li, Crystal structure and formation mechanism of $(Cr_{2/3}Ti_{1/3})_3AlC_2$ MAX phase, Acta Mater. 73 (2014) 186–193.

[12] H. Zhang, T. Hu, X.H. Wang, Y.C. Zhou, Structural defects in MAX phases and their derivative MXenes: A look forward, J. Mater. Sci. Technol. 38 (2020) 205–220.

[13] J. Xie, X.H. Wang, A.J. Li, F.Z. Li, Y.C. Zhou, Corrosion behavior of selected $M_{n+1}AXn$phases in hot concentrated HCl solution: Effect of a element and MX layer, Corros. Sci. 60 (2012) 129–135.

[14] M.A. Hadi, N. Kelaidis, S.H. Naqib, A. Chroneos, A.K. Islamae, Electronic structures, bonding natures and defect processes in Sn-based 211 MAX phases, Comp. Mater. Sci. 168 (2019) 203–212.

[15] K. Luo, X.H Zha, Q. Huang, C.T. Lin, R.F. Zhang, S.Y. Du, Theoretical

investigations on helium trapping in the Zr/Ti_2AlC interface, Surf. Coat. Tech. 322 (2017) 19–24.

[16] C. Kwakernaak, W.G. Sloof, Work of adhesion of interfaces between M_2AlC (M=Ti, V, Cr) MAX phases and α-Al_2O_3, Ceram. Int. 44 (2018) 23172–23179.

[17] M. Roknuzzaman, M.A. Hadi, M.A. Ali, M.M. Hossain, N. Jahan, M.M. Uddin, J.A. Alarco, K. Ostrikov, First hafnium-based MAX phase in the 312 family, Hf_3AlC_2: A first-principles study, J. Alloy. Compd. 727 (2017) 616–626.

[18] J.L. Nie, S.S. Liu, X.F. Zhan, L. Ao, L. Li, First-principles study of Hf/Nb/Zr-doped MAX phases Ti_3AlC_2 and Ti_3SiC_2, Physica B. 571 (2019) 105–111.

[19] P.A. Burr, D. Horlait, W.E. Lee, Experimental and DFT investigation of $(Cr,Ti)_3AlC_2$ MAX phases stability, Mater. Res. Lett. 5 (2017) 144–157.

[20] D. Bowden, J. Ward, S. Middleburgh, S. Shubeita, E. Zapata-Solvas, T. Lapauw, J. Vleugels, K. Lambrinoug, W.E. Lee, M. Preuss, P. Frankela, The stability of irradiation-induced defects in Zr_3AlC_2, Nb_4AlC_3 and $(Zr_{0.5},Ti_{0.5})3AlC_2$ MAX phase-based ceramics, Acta Mater. 183 (2020) 24–35.

[21] C.F. Hu, F.Z. Li, J. Zhang, J.M. Wang, J.Y. Wang, Y.C. Zhou, Nb_4AlC_3: A new compound belonging to the MAX phases, Scripta Mater. 57 (2007) 893–896.

[22] J.M. Wang, J.Y. Wang, Y.C. Zhou, C.F. Hu, Phase stability, electronic structure and mechanical properties of ternary-layered carbide Nb_4AlC_3: An ab initio study, Acta Mater. 56(2008) 1511–1518.

[23] B. YamanIslak, E. Ayas, Evaluation of properties of spark plasma sintered Ti_3SiC_2 and Ti_3SiC_2/SiC composites, Ceram. Int. 45 (2019) 12297–12306.

[24] H. Zhang, Z.J. Li, C. Zhang, J.L. Li, X.H. Wang, Y.C. Zhou, Nb doping in Ti_3AlC_2: Effects on phase stability, high-temperature compressive properties and oxidation resistance, J. Eur. Ceram. Soc. 37 (2017) 3641–3645.

[25] M. Radovic, M.W. Barsoum, A. Ganguly, T. Zhen, P. Finkel, S.R. Kalidindi, E. Lara-Curzio, On the elastic properties and mechanical damping of Ti_3SiC_2, Ti_3GeC_2, $Ti_3Si_{0.5}Al_{0.5}C_2$ and Ti_2AlC in the 300–1573 K temperature range, Acta Mater. 54 (2006) 2757–2767.

[26] Y. Wang, X.F. Wu, Z.W. Yang, Y.H. Xia, D.P. Wang, Microstructure and

mechanical properties of Ti_3SiC_2/Ti_3SiC_2 diffusion bonded joints using Ti foil as an interlayer, Ceram. Int. 45 (2019) 20900–20909.

[27] P. Istomin, E. Istomina, A. Nadutkin, V. Grass, Fabrication of Ti_3SiC_2/SiC_p multiport minichannel plates for high-temperature applications, J. Eur. Ceram. Soc. 39 (2019) 4602–4608.

[28] F.F. Qi, Z. Wang, J.Y. Wu, H.Q. Xu, J.J. Kou, L. Zhang, Improved mechanical properties of Al_2O_3 ceramic by in-suit generated Ti_3SiC_2 and TiC via hot pressing sintering, Ceram. Int. 43 (2017) 10691–10697.

[29] I.R. Shein, A.L. Ivanovskii, Planar nano-block structures $Ti_{n+1}Al_{0.5}C_n$ and $Ti_{n+1}C_n$ (n = 1, and 2) from MAX phases: Structural, electronic properties and relative stability from first principles calculations, Superlattice. Microst. 52 (2012) 147–157.

[30] M.A. Ali, M.M. Hossain, N. Jahan, A.K.M.A. Islam, S.H. Naqi, Newly synthesized Zr_2AlC, $Zr_2(Al_{0.58}Bi_{0.42})C$, $Zr_2(Al_{0.2}Sn_{0.8})C$, and $Zr_2(Al_{0.3}Sb_{0.7})C$ MAX phases: A DFT based first-principles study, Comp. Mater. Sci. 131 (2017) 139–145.

[31] E.Z. Solvas, M.A. Hadi, D. Horlait, D.C. Parfitt, A. Thibaud, A. Chroneos, W.E. Lee, Synthesis and physical properties of $(Zr_{1-x},Ti_x)_3AlC_2$ MAX phases, J. Am. Ceram. Soc. 100 (2017) 3393–3401.

[32] X.H. Zhang, Y.F. Li, Y.J. Qiao, H.L. Chen, Y. Wang, T.C. Germanne, Q. Huang, X.J. Bai, X.B. Zhou, Y.L. Guo, K. Luo, S.Y. Du, First-principles study on the stability and properties of β-SiC/$M_{n+1}AlC_n$ (M=Sc, Ti, V, Cr, Zr, Nb, Mo, Hf, Ta; n=1,2) interfaces, J. Phys. Chem. Solids. 127 (2019) 119–126.

[33] H.Z. Zhang, S.Q. Wang, First-principles study of Ti_3AC_2 (A = Si, Al) (001) surfaces, Acta Mater. 55 (2007) 4645–4655.

Figures

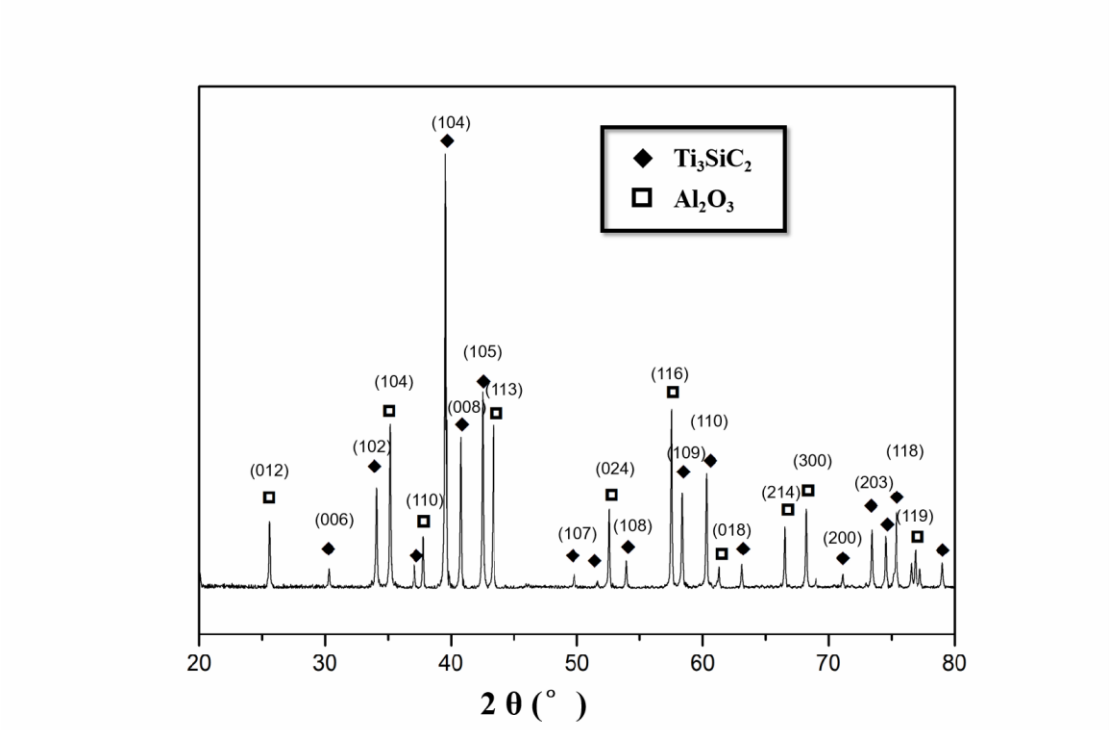

Fig. 1. XRD patterns of Ti_3SiC_2/Al_2O_3 ceramics.

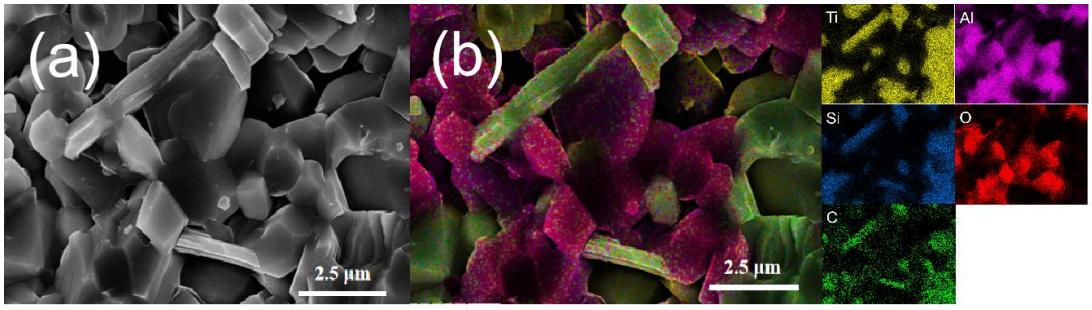

Fig. 2. (a) SEM and (b) EDS images of Ti_3SiC_2/Al_2O_3 ceramics.

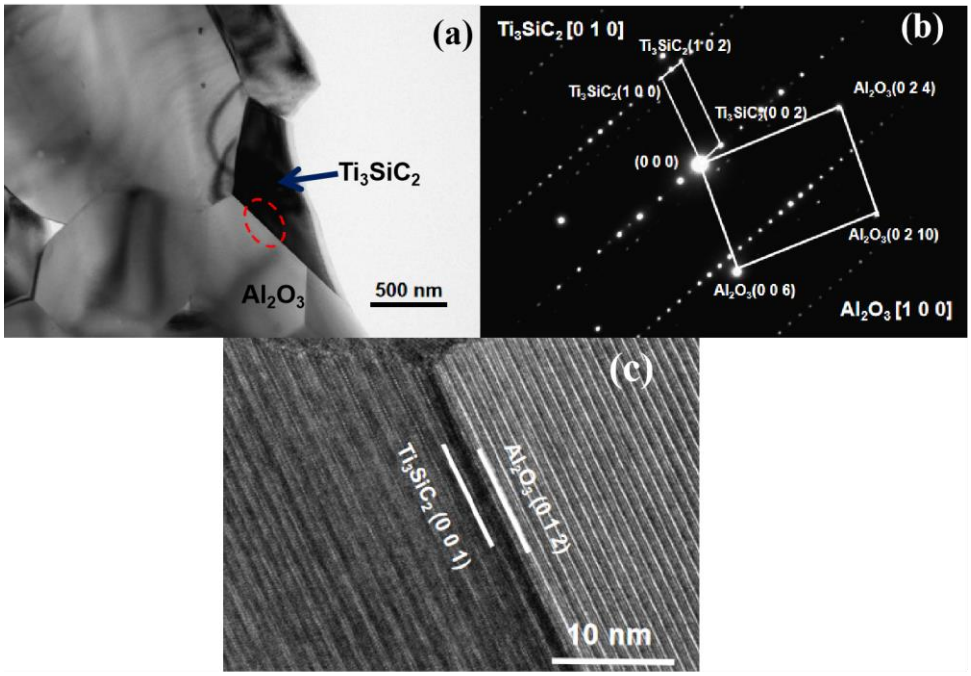

Fig. 3. (a) Bright-field TEM figures of Ti_3SiC_2‖ Al_2O_3 interface. (b) SAED pattern of Ti_3SiC_2‖ Al_2O_3 interface. (c) Lattice fringes of the Ti_3SiC_2 (001) and Al_2O_3 (012) planes.

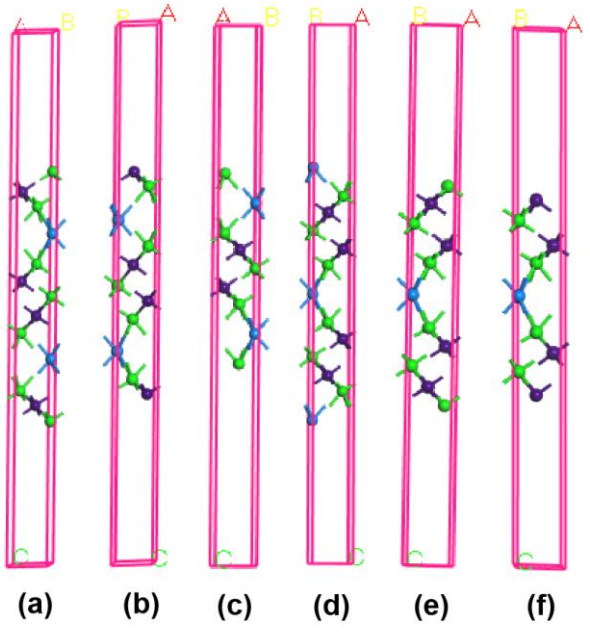

Fig. 4. Structural models of the Ti_3SiC_2 (001) plane with different terminations (green: Ti; bule: Si; purple: C). (a) Ti1(C); (b) C(Ti2); (c)Ti2(Si); (d) Si(Ti2); (e) Ti2(C); and (f) C(Ti1).

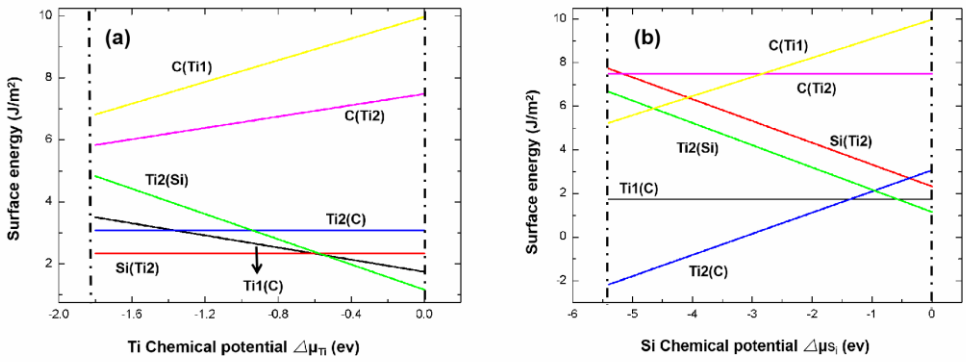

Fig. 5. Surface energies upon variation in the chemical potentials. (a) and (b) Surface energy of Ti_3SiC_2 (001) as a function of $\Delta\mu_{Ti}$ and $\Delta\mu_{Si}$, respectively.

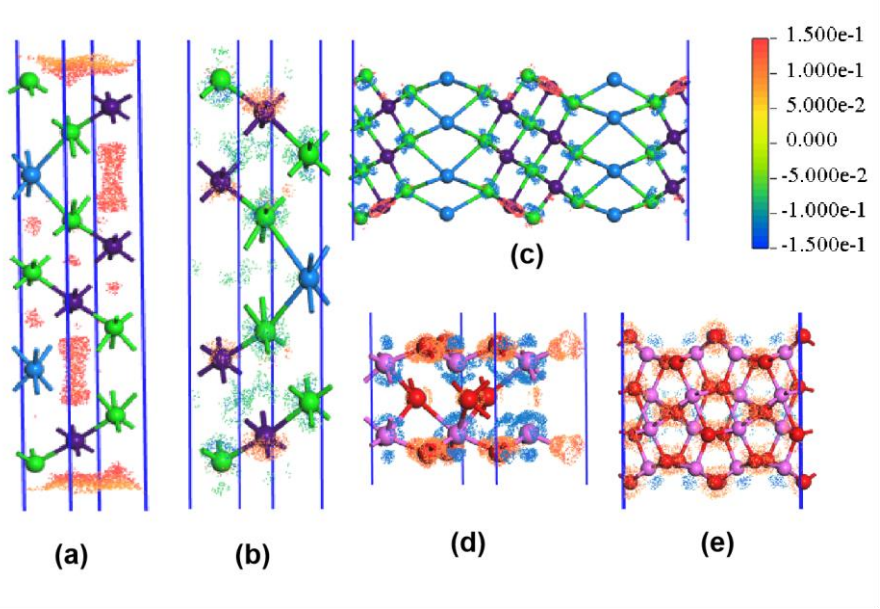

Fig. 6. Electron density differences for the Ti_3SiC_2 and Al_2O_3 crystal surfaces (green: Ti; bule: Si; purple: C; pink: Al; red: O). (a):TSC(001)-Ti1; (b) TSC(001)-Ti2; (c) TSC(100); (d) AO(001); and (e) AO(012).

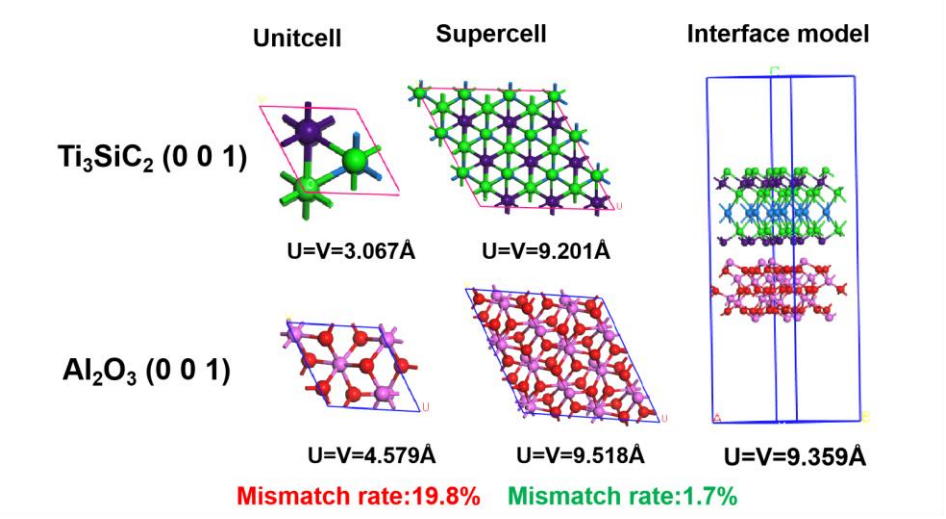

Fig. 7. Unit cell and supercell models of Ti_3SiC_2 and Al_2O_3 with different mismatch rates.

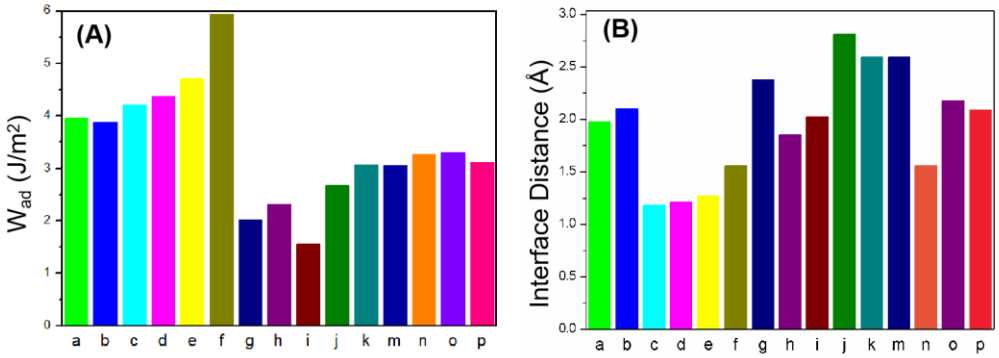

Fig. 8. (A) W_{ad} values and (B) interface distances for the fifteen interface models. (a)TSC (001)-Ti1‖ AO (001); (b)TSC (001)-Ti2‖ AO (001); (c)TSC (100)‖ AO (001); (d)TSC (001)-Ti1‖ AO (012); (e)TSC (001)-Ti2‖ AO (012); (f) TSC (100)‖ AO (012); (g)AO (001)‖ AO (001); (h)AO (012)‖ AO (012); (i) AO (001)‖ AO (012); (j) TSC (001)-Ti1‖ TSC (001)-Ti1; (k)TSC (001)-Ti2‖ TSC (001)-Ti2; (m)TSC (001)-Ti1‖ TSC (001)-Ti2; (n) TSC (100)‖ TSC (100); (o)TSC (001)-Ti1‖ TSC (100); and (p)TSC (001)-Ti2‖ TSC (100).

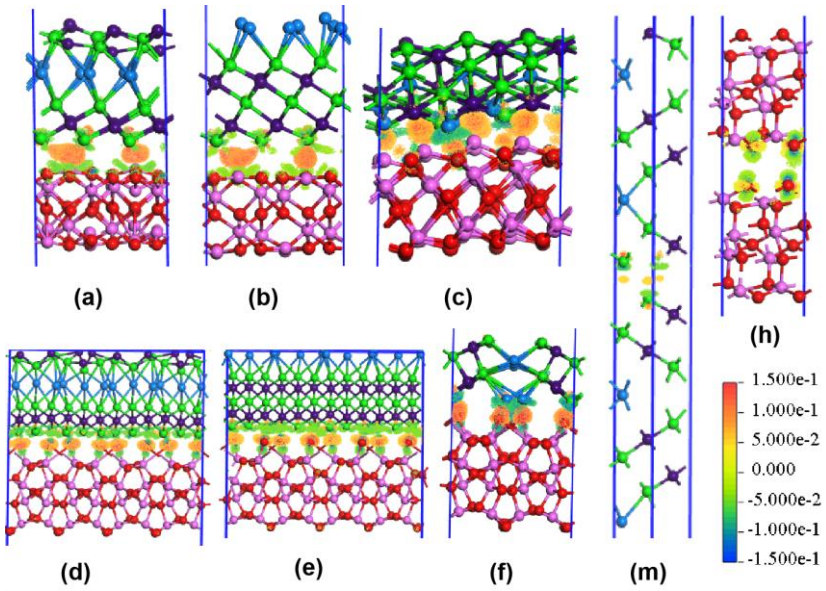

Fig. 9. Differences in electron density of eight interface models (green: Ti; bule: Si; purple: C; pink: Al; red: O). (a)TSC (001)-Ti1‖ AO (001); (b)TSC (001)-Ti2‖ AO (001); (c)TSC (100)‖ AO (001); (d)TSC (001)-Ti1‖ AO (012); (e)TSC (001)-Ti2‖ AO (012); (f) TSC (100)‖ AO (012); (h)AO (012)‖ AO (012); (m)TSC (001)-Ti1‖ TSC (001)-Ti2;